

# UC Berkeley

## UC Berkeley Previously Published Works

### Title

Recent methane surges reveal heightened emissions from tropical inundated areas.

### Permalink

<https://escholarship.org/uc/item/6762s74h>

### Journal

Nature Communications, 15(1)

### Authors

Lin, Xin

Peng, Shushi

Ciais, Philippe

et al.

### Publication Date

2024-12-30

### DOI

10.1038/s41467-024-55266-y

Peer reviewed

# Recent methane surges reveal heightened emissions from tropical inundated areas

Received: 3 August 2023

Accepted: 4 December 2024

Published online: 30 December 2024

 Check for updates

Xin Lin<sup>1</sup>✉, Shushi Peng<sup>2</sup>, Philippe Ciais<sup>1,3</sup>, Didier Hauglustaine<sup>1</sup>, Xin Lan<sup>4,5</sup>, Gang Liu<sup>2</sup>, Michel Ramonet<sup>1</sup>, Yi Xi<sup>1,2</sup>, Yi Yin<sup>6</sup>, Zhen Zhang<sup>7</sup>, Hartmut Bösch<sup>8</sup>, Philippe Bousquet<sup>1</sup>, Frédéric Chevallier<sup>1</sup>, Bogang Dong<sup>2</sup>, Cynthia Gerlein-Safdi<sup>9</sup>, Santanu Halder<sup>1</sup>, Robert J. Parker<sup>10,11</sup>, Benjamin Poulter<sup>12</sup>, Tianjiao Pu<sup>9</sup>, Marine Remaud<sup>1</sup>, Alexandra Runge<sup>13</sup>, Marielle Saunois<sup>1</sup>, Rona L. Thompson<sup>14</sup>, Yukio Yoshida<sup>15</sup> & Bo Zheng<sup>16,17</sup>

Record breaking atmospheric methane growth rates were observed in 2020 and 2021 ( $15.2 \pm 0.5$  and  $17.8 \pm 0.5$  parts per billion per year), the highest since the early 1980s. Here we use an ensemble of atmospheric inversions informed by surface or satellite methane observations to infer emission changes during these two years relative to 2019. Results show global methane emissions increased by  $20.3 \pm 9.9$  and  $24.8 \pm 3.1$  teragrams per year in 2020 and 2021, dominated by heightened emissions from tropical and boreal inundated areas, aligning with rising groundwater storage and regional warming. Current process-based wetland models fail to capture the tropical emission surges revealed by atmospheric inversions, likely due to inaccurate representation of wetland extents and associated methane emissions. Our findings underscore the critical role of tropical inundated areas in the recent methane emission surges and highlight the need to integrate multiple data streams and modeling tools for better constraining tropical wetland emissions.

In the years 2020 and 2021, the methane growth rate (MGR) in the atmosphere reached  $15.2 \pm 0.5$  and  $17.8 \pm 0.5$  parts per billion per year ( $\text{ppb yr}^{-1}$ ) respectively, hitting record highs since systematic measurements started in the early 1980s by NOAA's Global Monitoring Laboratory (GML)<sup>1</sup>. The unprecedented methane growth during 2020 and 2021 coincided with the reduced human activities and pollutant

emissions during COVID-19 lockdowns and the gradual recovery afterwards<sup>2–5</sup>, together with the occurrence of a moderate and prolonged La Niña event<sup>6</sup>, which offers a unique opportunity to examine the drivers of methane variabilities on a year-to-year basis.

Both process-based studies of sources (“bottom-up” estimates) and atmospheric-based inverse analyses (“top-down” estimates)

<sup>1</sup>Laboratoire des Sciences du Climat et de l'Environnement, LSCE/IPSL, CEA-CNRS-UVSQ, Université Paris-Saclay, Gif-sur-Yvette, France. <sup>2</sup>Sino-French Institute for Earth System Science, College of Urban and Environmental Sciences, Peking University, Beijing, China. <sup>3</sup>Climate and Atmosphere Research Center (CARE-C), The Cyprus Institute, Nicosia, Cyprus. <sup>4</sup>Cooperative Institute for Research in Environmental Sciences of University of Colorado, Boulder, CO, USA. <sup>5</sup>Global Monitoring Laboratory, National Oceanic and Atmospheric Administration, Boulder, CO, USA. <sup>6</sup>Department of Environmental Studies, New York University, New York, NY, USA. <sup>7</sup>National Tibetan Plateau Data Centre, State Key Laboratory of Tibetan Plateau Earth System, Environment and Resource, Institute of Tibetan Plateau Research, Chinese Academy of Sciences, Beijing, China. <sup>8</sup>Institute of Environmental Physics, University of Bremen, Bremen, Germany. <sup>9</sup>Department of Civil and Environmental Engineering, University of California, Berkeley, CA, USA. <sup>10</sup>National Centre for Earth Observation, Space Park Leicester, University of Leicester, Leicester, UK. <sup>11</sup>Earth Observation Science, School of Physics and Astronomy, University of Leicester, Leicester, UK. <sup>12</sup>Biospheric Sciences Laboratory, NASA Goddard Space Flight Center, Greenbelt, MD, USA. <sup>13</sup>Alfred Wegener Institute, Helmholtz Centre for Polar and Marine Research, Potsdam, Germany. <sup>14</sup>NILU, Kjeller, Norway. <sup>15</sup>National Institute for Environmental Studies, Tsukuba, Japan. <sup>16</sup>Institute of Environment and Ecology, Tsinghua Shenzhen International Graduate School, Tsinghua University, Shenzhen, China. <sup>17</sup>State Environmental Protection Key Laboratory of Sources and Control of Air Pollution Complex, Beijing, China. ✉e-mail: [xinlin.res@gmail.com](mailto:xinlin.res@gmail.com)

pointed to pronounced emission growth in 2020 compared to 2019, arising from tropical and northern sources, likely driven by enhanced wetland emissions<sup>7–10</sup>, the main source component of natural methane emissions. From 2019 to 2020, the increase of MGR was earlier and larger in the Tropics and Northern high-latitudes than in the Southern extra-tropics from NOAA GML marine boundary layer sites (Figs. 1b and S1; see Methods)<sup>11</sup>, consistent with an activation of wetland emissions. The exceptionally high methane growth persisted in 2021, and prevailed over most latitude bands (Fig. 1a, b). Observations of total column methane concentrations (XCH<sub>4</sub>) by Greenhouse Gases

Observing SATellite (GOSAT), whether obtained from the National Institute for Environmental Studies (Japan) full physics retrievals (hereafter “GSNIES”)<sup>12</sup> or from the University of Leicester proxy retrievals (hereafter “GSUoL”)<sup>13</sup>, confirmed the unexpected methane surges in 2020 and 2021 (Fig. 1c, d). Note that both GOSAT retrievals showed a larger MGR increase in 2020 over the Southern extra-tropics than that observed from surface network, with GSUoL exhibiting higher MGR globally and in the Tropics as well (Figs. 1 and S1).

The zonally-averaged changes in MGR across latitude bands reveal the integrated variations of regional sources and sinks, atmospheric transport, and removal by the hydroxyl radical (OH). In this study, we use a global atmospheric inversion system (PYVAR-LMDZ-SACS; see Methods)<sup>14,15</sup> that assimilated either surface or satellite-based CH<sub>4</sub> observations to infer the spatiotemporal patterns in flux changes from 2019 to 2021. An ensemble of six inversions is performed, with different assimilated observation datasets (surface network, GSNIES or GSUoL) and transport model physical parameterizations (the “classic” and “advanced” versions) (Table S1; see Methods). This allows us to test the consistency of flux change patterns inferred from different types of measurements while accounting for the uncertainties due to imperfect representation of atmospheric mixing. Surface networks offer a good coverage of northern mid-to-high latitudes (especially over Europe and North America), whereas satellite data have improved data densities from 60°S to 60°N, particularly a better coverage of the tropics than surface networks (Figs. S2 and S3). We prescribe changes in OH concentration fields from a full chemistry transport model (LMDZ-INCA)<sup>16,17</sup>, driven by interannually varying meteorology<sup>18</sup> with natural and anthropogenic emissions of NO<sub>x</sub>, CO and hydrocarbons updated to 2021 (Fig. S4; Table S2; see Methods)<sup>19–21</sup>. The ensemble of atmospheric inversions reveals anomalous and persistent emission surges from inundated areas in tropical Africa and Asia during 2020–2021, linked to water table rises and La Niña conditions. Meanwhile, we also quantify variations of methane emissions using bottom-up inventories for anthropogenic and fire sources, and process-based biogeochemical models for wetland emissions (see Methods). We find that the strong emission enhancements over tropical inundated areas are not captured by current process-based wetland models, likely pointing to models’ limitations in accurately representing dynamics of tropical wetland extents and processes driving tropical wetland methane emissions.

## Results and Discussions

### Variations of methane emissions from atmospheric inversions

All members of the ensemble of six inversions showed global increases in surface CH<sub>4</sub> emissions by an average of 20.3±9.9 Tg CH<sub>4</sub> yr<sup>-1</sup> and 24.8±3.1 Tg CH<sub>4</sub> yr<sup>-1</sup> in 2020 and 2021 respectively, compared to 2019 (uncertainty being one standard deviation of the ensemble). A large portion of this surge in global emissions was accounted for by the northern tropics (0°–30°N), which contributed about 80% (16.2±8.3 Tg CH<sub>4</sub> yr<sup>-1</sup>) and 95% (23.2±4.0 Tg CH<sub>4</sub> yr<sup>-1</sup>) of the global increases in 2020 and 2021, respectively (Figs. 2a, b and S5; Table S3). Higher emission increases were found over tropical Africa and Southeast Asia in both years, according to all six inversions (Figs. 2a, b and S5–S7). Overall, most of the regions with strong and consistent emission changes overlapped with major wetland complexes and inundated areas. These emission anomalies aligned well with changes in liquid water equivalent (LWE) from the Gravity Recovery and Climate Experiment Follow-On (GRACE-FO) satellites (Figs. 2a–d and S5c–f). LWE is a proxy for water-table depth and water stored in wetland systems<sup>22</sup>.

Focusing on the 20 major wetland regions of the globe that represent about 60% of all wetland areas based on the map of ref. 23, a significant correlation was noted between top-down estimates of emission anomalies and changes in LWE from GRACE-FO (Fig. 2e–g). The correlation with temperature or precipitation changes was not statistically significant across regions (Fig. S8), although these two factors

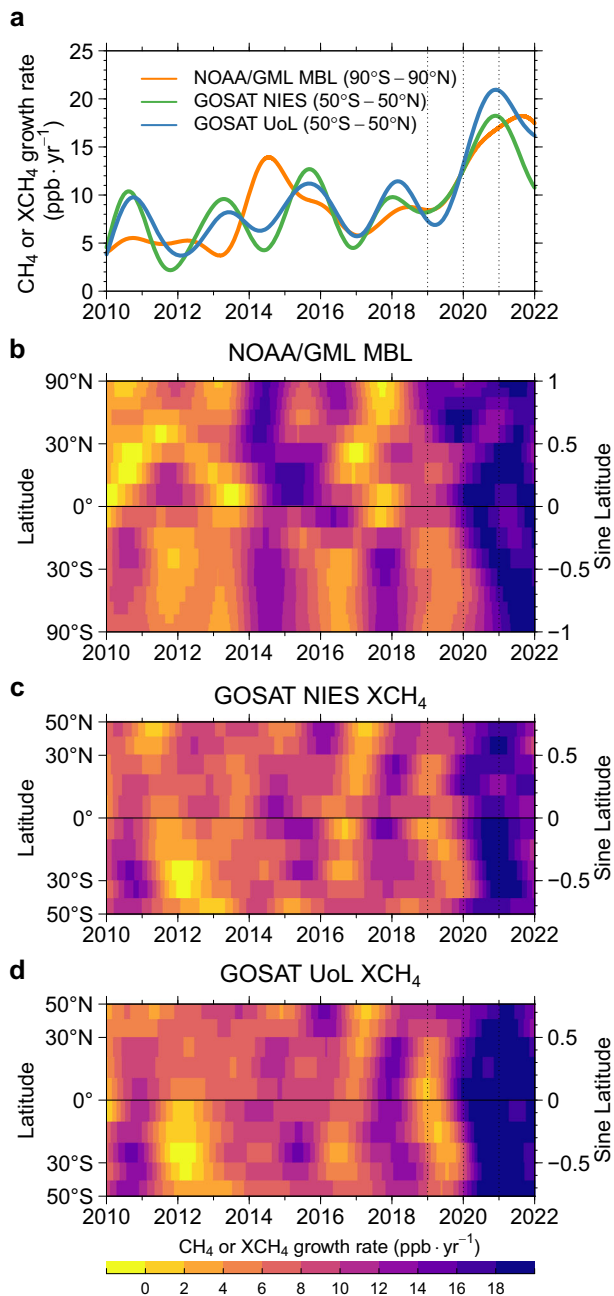


**Fig. 1 | Variations of atmospheric methane growth rates between 2010 and 2021.** **a–d** Methane (CH<sub>4</sub>) growth rates were derived from zonally averaged observations of NOAA Global Monitor Laboratory (NOAA/GML) marine boundary layer (MBL) sites<sup>11</sup>, GOSAT NIES retrievals<sup>12</sup> or GOSAT UoL retrievals<sup>13</sup> of total column methane concentrations (XCH<sub>4</sub>), following the curve-fitting routines of ref. 71. For **c**, **d**, results are not shown north of 50°N or south of 50°S due to data gaps of GOSAT retrievals over these regions during winter. Source data are provided as a Source Data file.

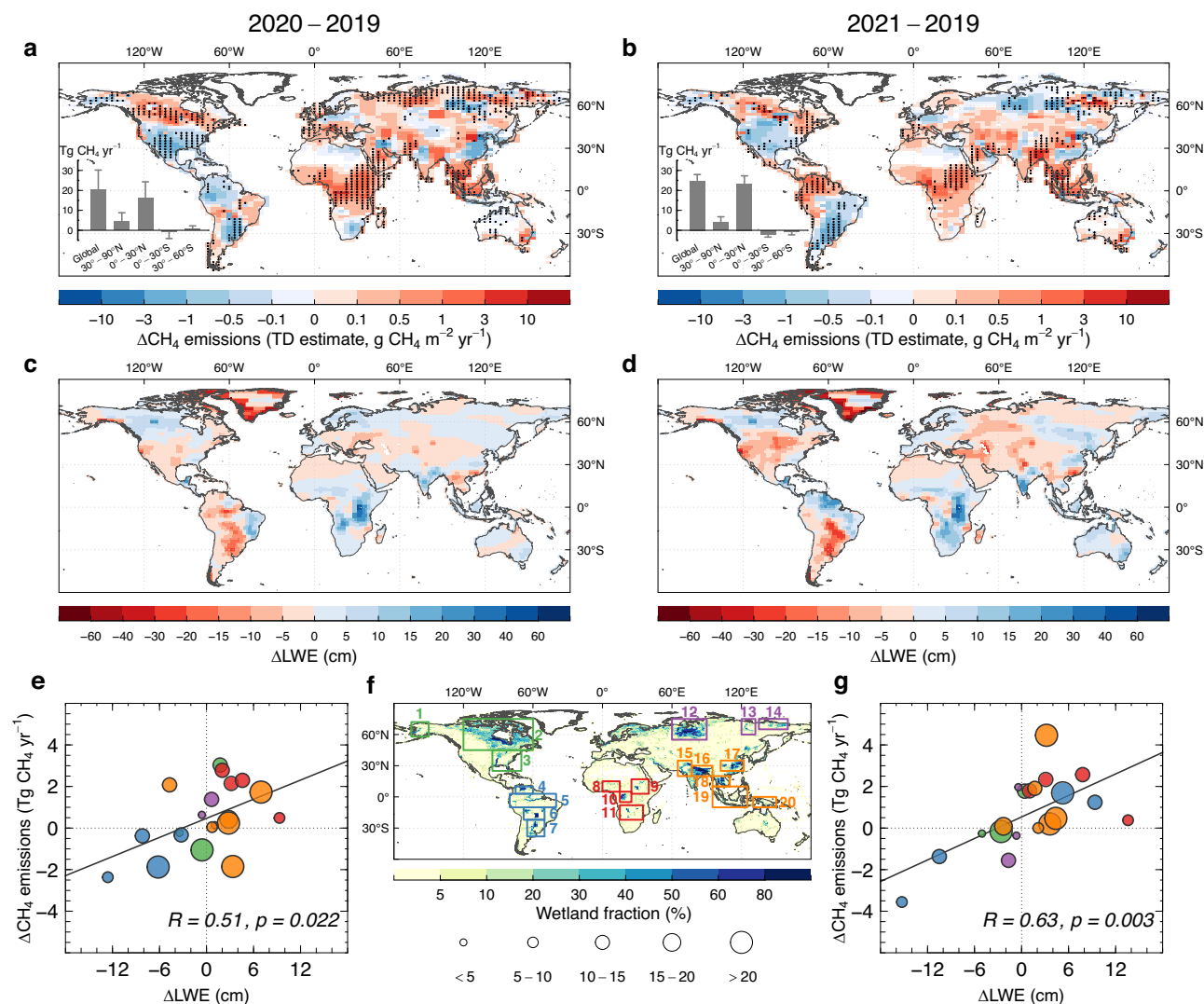


**Fig. 2 | Methane emission anomalies in 2020 and 2021 relative to 2019 inferred from six inversions in relation to changes in satellite observed liquid water equivalent (LWE). a, b** Spatial patterns of the mean  $\text{CH}_4$  emission anomalies ( $\Delta\text{CH}_4$  emissions) averaged over the ensemble of six top-down (TD) inversions. The shaded areas indicate that posterior fluxes from all six inversions have the same changing direction. The inset bar plots summarize the net emission changes at the global scale and for four latitude bands. Error bars represent one standard

deviation of the six inversions. **c, d** Spatial patterns of changes in LWE ( $\Delta\text{LWE}$ ) from the GRACE-FO satellites. **e, g** Scatterplot of  $\text{CH}_4$  emission anomalies versus changes in GRACE-FO LWE across 20 major wetland regions defined based on the regularly flooded wetland map<sup>23</sup> in **f**. Each circle represents a major wetland region, with the size scaling with the magnitude of the region's posterior methane emission in 2019 (unit:  $\text{Tg CH}_4 \text{ yr}^{-1}$ ). The color of the circle corresponds to the color code for each wetland region in **f**. Source data are provided as a Source Data file.

could potentially impact emission variations between years for individual wetland regions (Table S4). Among the 20 wetland regions, the Niger River basin, the Congo basin, the Sudd swamp, the Ganges floodplains and the Southeast Asian deltas in the tropics, and the Hudson Bay lowlands in the boreal region, exhibited persistent emission enhancements in both 2020 and 2021. Emission increases over each of these regions exceeded by at least 1.5–2 times the interannual variability ( $1.5\text{--}2\sigma$ ) of methane emissions during 2010–2019 (Table S5), based on the results of inversions with settings comparable to those in our study but covering a longer period<sup>24</sup>. These six wetland regions together contributed around 70% ( $14.1 \pm 4.2 \text{ Tg CH}_4 \text{ yr}^{-1}$ ) and 60% ( $14.9 \pm 2.6 \text{ Tg CH}_4 \text{ yr}^{-1}$ ) of the global emission increases for 2020 and 2021, respectively (Figs. 2, 3e, f and S5; Table S5). The synchronous emission increases over these wetland regions were paralleled by overall wetter conditions (increased LWE or precipitation), and additionally by warming conditions for specific regions (e.g., Hudson Bay lowlands; Table S4).

Substantial emission increases were also found over the western Siberian lowlands in 2020 and the Amazon Basin and the Orinoco

floodplain in 2021, but reduced emissions were seen in the other years over these regions (i.e., the western Siberian lowlands in 2021; the Amazon Basin and the Orinoco floodplain in 2020), aligning with corresponding variations in temperature and/or LWE (Figs. 2, 3e, f, and S5; Table S4). For the Amazon Basin in particular, the enhanced emissions in 2021 were associated with increased floodplain inundation and the record high water levels<sup>25</sup>, linked to intense rainfall over the northern Amazonia driven by the La Niña conditions, with strengthened Walker circulation and deep convection<sup>26,27</sup>. Conversely, the Pantanal and the Paraná floodplains in central and southeastern South America exhibited emission reduction in both 2020 and 2021, due to continued drier conditions and lower water tables (Figs. 2, 3e, f and S5; Table S4). These two regions experienced severe and prolonged drought events since 2019, leading to record low water levels over the past decades<sup>28–30</sup> and therefore persistent reduction in  $\text{CH}_4$  emissions.

The overall strong emission increases over tropical inundated areas were coincident with the occurrence of a prolonged La Niña

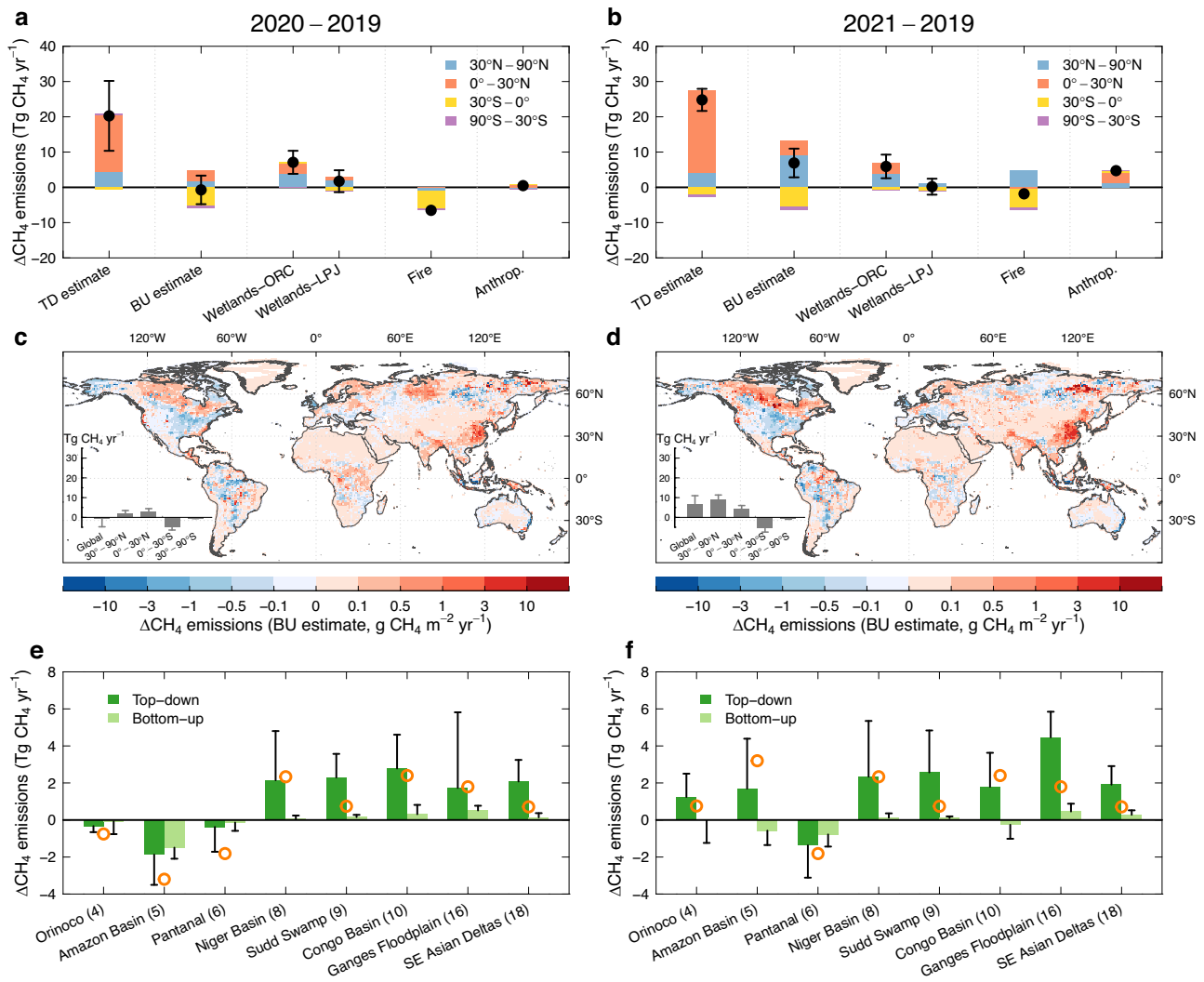


**Fig. 3 | Top-down versus bottom-up estimates of methane emission anomalies in 2020 and 2021 relative to 2019.** **a, b** Mean methane emission anomalies ( $\Delta\text{CH}_4$  emissions) of four latitude bands derived from the ensemble of six top-down (TD) inversions and bottom-up (BU) estimates. The black dots represent the net global emission changes relative to 2019. **c, d** Spatial patterns of bottom-up  $\text{CH}_4$  emission anomalies summed up from process-based wetland models, and inventories of anthropogenic and fire emissions. The color scale is the same as for the top-down  $\text{CH}_4$  emission anomalies in Fig. 2a, b. The inset bar plots summarize the net emission changes at the global scale and for four latitude bands. **e, f** Top-down versus

bottom-up estimates of methane emission anomalies for eight tropical inundated areas. The delineation of each inundated area is shown in Fig. 2f and Fig. S5i. The open circle indicates two times the interannual variability ( $+2\sigma$  or  $-2\sigma$ ) of methane emissions during 2010–2019 derived from a previous study using the inversion system PYVAR-LMDZ-SACS and GSUoL as constraints for  $\text{CH}_4$  (ref. 24). Error bars in all panels denote one standard deviation of the methane emission anomalies from the ensemble of top-down or bottom-up estimates. Source data are provided as a Source Data file.

event since 2020. La Niña is the cold phase of the El Niño–Southern Oscillation (ENSO) cycles—the dominant mode of interannual climate variability impacting weather patterns and ecosystem dynamics across the globe. La Niña is generally associated with a wetter climate and above-normal precipitation over tropical land areas<sup>31</sup>, which correlates with higher wetland methane emissions through expanded flooded areas. Previous studies suggested a broad anti-correlation between wetland  $\text{CH}_4$  emissions and ENSO at the global and pan-tropical scales, with less emissions during strong El Niño events and more emissions during strong La Niña events (Fig. S9; also see refs. 32–35). At the regional scales, however, the sign, magnitude and phasing of wetland responses to ENSO could vary<sup>32,34,35</sup> depending on the spatiotemporal variability in climate anomalies during specific ENSO episodes<sup>36</sup>, which complicates the relationship between ENSO, wetland  $\text{CH}_4$  emissions, and  $\text{CH}_4$  growth rates<sup>37</sup>. Our results covering the most recent La Niña episode confirm the overall enhanced  $\text{CH}_4$  emissions over inundated areas during La Niña conditions, and further demonstrate the diverse

response patterns across regions and between years that could be linked to the complex evolution of ENSO-related climate anomalies.

### Bottom-up estimates of methane emission changes

Bottom-up inventories and process-based wetland emission models independently corroborate increased emissions over the northern tropics during 2020–2021, albeit with much smaller magnitudes than inversions (Figs. 2, 3 and S10; Table S3). Globally, the net emission changes were  $-0.7 \pm 4.0 \text{ Tg CH}_4 \text{ yr}^{-1}$  and  $6.9 \pm 4.1 \text{ Tg CH}_4 \text{ yr}^{-1}$  in 2020 and 2021 relative to 2019 based on bottom-up methodologies, with emission increases of  $3.2 \pm 1.3 \text{ Tg CH}_4 \text{ yr}^{-1}$  and  $4.1 \pm 1.9 \text{ Tg CH}_4 \text{ yr}^{-1}$  estimated for the northern tropics (Figs. 3a, b and S10; Table S3). A breakdown into different processes showed that the anthropogenic  $\text{CH}_4$  emissions in 2020 and 2021 were higher than the 2019 level by  $0.5 \text{ Tg CH}_4 \text{ yr}^{-1}$  and  $4.7 \text{ Tg CH}_4 \text{ yr}^{-1}$ , respectively (Fig. S10; Table S3). While fossil fuel  $\text{CH}_4$  emissions were reduced during COVID-19 lockdowns and rebounded partially afterwards (by  $-2.7 \text{ Tg CH}_4 \text{ yr}^{-1}$  and  $-0.5 \text{ Tg}$

$\text{CH}_4$   $\text{yr}^{-1}$  for 2020 and 2021 compared to 2019), the  $\text{CH}_4$  biogenic emissions from sectors of agriculture and waste treatment continued to increase (by 3.1 Tg  $\text{CH}_4$   $\text{yr}^{-1}$  and 5.2 Tg  $\text{CH}_4$   $\text{yr}^{-1}$  for 2020 and 2021 compared to 2019), leading to a net increase of anthropogenic emissions. The global fire  $\text{CH}_4$  emissions declined in 2020 by 6.5 Tg  $\text{CH}_4$   $\text{yr}^{-1}$  relative to 2019, mainly contributed by reduced fire emissions of 5.1 Tg  $\text{CH}_4$   $\text{yr}^{-1}$  in the southern tropics (30°S–0°)<sup>21</sup>. A similar reduction of fire emissions occurred again in the southern tropics in 2021, but the extreme fires in boreal North America and eastern Siberia during the hotter and drier summertime<sup>38</sup> led to an increase in emissions of 4.7 Tg  $\text{CH}_4$   $\text{yr}^{-1}$  in the northern extra-tropics and therefore a net global emission reduction of only 1.8 Tg  $\text{CH}_4$   $\text{yr}^{-1}$  relative to 2019 (Figs. 3a, b and S10; Table S3). For wetlands, the results of process-based wetland model simulations from ORCHIDEE-MICT and LPJ-wsl driven by four different climate forcings (see Methods) reported an increase in global wetland emissions by  $5.3 \pm 4.0$  Tg  $\text{CH}_4$   $\text{yr}^{-1}$  in 2020 compared to 2019, which was dominated by enhanced wetland emissions in the northern extra-tropics and tropics as a result of warmer and wetter climate<sup>8</sup>. The updated simulations showed slightly smaller wetland emission increases by  $4.0 \pm 4.1$  Tg  $\text{CH}_4$   $\text{yr}^{-1}$  in 2021 compared to 2019, with similar latitudinal patterns (Figs. 3a, b, S10 and S11; Table S3).

Given differences of simulated wetland emissions by process-based biogeochemical models (Fig. S11), the global total emission increases from the bottom-up approach were much lower than those from inversions. When the maximum wetland emission increases are considered (i.e., 13.4 Tg  $\text{CH}_4$   $\text{yr}^{-1}$  and 11.5 Tg  $\text{CH}_4$   $\text{yr}^{-1}$  in 2020 and 2021 by ORCHIDEE-RFW with MERRA2; Fig. S11), the total emission increases amounted to 7.4 Tg  $\text{CH}_4$   $\text{yr}^{-1}$  and 14.4 Tg  $\text{CH}_4$   $\text{yr}^{-1}$  in 2020 and 2021, respectively, still 12.9 Tg  $\text{CH}_4$   $\text{yr}^{-1}$  and 10.4 Tg  $\text{CH}_4$   $\text{yr}^{-1}$  below the mean of the inversion ensemble estimates. While there was a general agreement in the broad spatial patterns of emission changes between the bottom-up and top-down approaches, large underestimation by the bottom-up approach was found over the tropics, especially in tropical Africa and Asia (Figs. 2, 3 and S10). Specifically, for the Niger River basin, the Congo basin, the Sudd swamp, the Ganges floodplains and the Southeast Asian deltas, the total emission increases from the bottom-up approach only accounted for 11% and 5% of the estimates from top-down inversions for 2020 and 2021, respectively (Fig. 3e, f; Table S5).

The lower bottom-up estimates of emission increases over tropical Africa and Asia inundated areas suggest that wetland biogeochemical models may misrepresent key processes in wetland dynamics and associated changes in  $\text{CH}_4$  emissions. A close look into the Sudd swamp, the wetland emission hotspot in the eastern Africa (3°N–17°N, 25°E–40°E; see also refs. 39–41) showed that the annual variations in top-down  $\text{CH}_4$  emissions and GRACE-FO LWL anomalies were highly correlated (Fig. S12), implying a strong impact of water-table depth on seasonal emissions over tropical inundated areas (Fig. S13; see also refs. 22,39,42). The annual peak of LWL occurs during September–October, about one month before the annual peak of emissions from top-down inversions. The seasonal peak of emissions during September–November in Sudd (about 0.3 Tg  $\text{CH}_4$  month<sup>-1</sup> higher relative to April–June) is missed by most wetland model simulations (giving only a non-significant rise of 0.02 Tg  $\text{CH}_4$  month<sup>-1</sup> during September–November relative to April–June; Fig. S12). This could be partly explained by the simulation of too small wetland extents of the Sudd swamp and weak intra- and inter-annual variations, as shown by the comparison between the simulated flooded areas and high-resolution observations from the CYGNSS satellites<sup>43,44</sup>. The too small seasonal changes in wetland extent and associated  $\text{CH}_4$  emissions were also identified previously in other process-based or data-driven wetland models over tropical regions<sup>33,41,45,46</sup>, resulting in smaller estimates of year-to-year emission anomalies. Besides, large uncertainties remain in the model representation of  $\text{CH}_4$  production, oxidation and vegetation-mediated transport processes for tropical

wetlands<sup>47,48</sup>, where direct flux measurements are sparse<sup>49,50</sup>. For example, field studies have demonstrated the importance of vegetation-mediated  $\text{CH}_4$  fluxes in tropical wetlands even when the water table is below the soil surface<sup>51</sup>. These processes have been considered in recent development of process-based wetland models but not calibrated for tropical wetlands due to lack of field measurements<sup>52</sup>. More observations of tropical wetland hydrology and associated  $\text{CH}_4$  emissions are thus needed to calibrate and constrain model parameterizations, thereby improving models' predictive capacity. It should be noted that other emissions from anthropogenic sources and biomass burning may co-exist in the inundated areas (Figs. S10 and S12). Estimation of these sources could also be uncertain and further contribute to the discrepancies between bottom-up and top-down estimates of emission anomalies.

In summary, the record high  $\text{CH}_4$  growth rates in 2020 and 2021 revealed heightened emissions from inundated areas in the tropical and boreal regions. Strong and persistent emission surges were found simultaneously over the Niger River basin, the Congo basin, the Sudd swamp, the Ganges floodplains, the Southeast Asian deltas, and Hudson Bay lowlands, coincident with elevated groundwater and warming in the north, and potentially linked to La Niña conditions prevailing since 2020. Our main findings on heightened emissions from both tropical and boreal wetlands, along with evidence from other bottom-up or top-down studies<sup>10,39,53–56</sup>, suggest recent intensification of wetland methane emissions and probable strong positive wetland climate feedback<sup>57</sup>. In a future with warming climate (unavoidable in the Arctic) and possibly increasing occurrences of extreme or prolonged La Niña events<sup>58,59</sup>, the synchronous emission rise across boreal and tropical wetlands, as seen in 2020 and 2021, may occur more frequently and has the potential to accelerate atmospheric  $\text{CH}_4$  growth. This would challenge the commitment of the Paris Agreement to limit global warming, and stresses the urgency of greater reduction in anthropogenic emissions to achieve climate mitigation goals<sup>57,60</sup>. Our study also adds key 'natural experiments' from La Niña conditions in 2020 and 2021 to better understand the complex spatial-temporal variations in wetland emissions linked to ENSO. A systematic evaluation of wetland responses and their asymmetry between El Niño and La Niña conditions will help identify fingerprint of ENSO-induced climate variability in wetland dynamics, and may eventually contribute to an improved characterization of future variations in wetland  $\text{CH}_4$  emissions and atmospheric  $\text{CH}_4$  growth rates. Current process-based wetland models fail to capture the strong emission surges over the tropics revealed by top-down inversions. Improved wetland extent mapping and modeling, informed by sustained and enhanced observations on wetland hydrology and biogeochemistry, will help constrain tropical wetland emissions under changing climate and reconcile  $\text{CH}_4$  budget estimation between bottom-up and top-down approaches.

## Methods

We followed the methodologies described in ref. 8 to combine both top-down and bottom-up approaches for a synthesis study of recent methane growth during 2020–2021. The analyses of methane emission changes were extended to 2021 on the basis of ref. 8 using similar data sources and modeling tools. We further included satellite-based  $\text{CH}_4$  observations and flux inversions in addition to the analyses derived from surface  $\text{CH}_4$  networks, which allows for intercomparison of the emission change patterns that are informed by different datasets of atmospheric  $\text{CH}_4$  observations.

## Atmospheric observations

For surface  $\text{CH}_4$  observations, in-situ continuous and flask-air  $\text{CH}_4$  measurements from a total of 121 stations for the inversion analyses were included (Fig. S2), most of which are operated and maintained by the NOAA<sup>61</sup> and Integrated Carbon Observation System<sup>62</sup>. Observations from other networks, including those from Environment and

Climate Change Canada (ECCC), Advanced Global Atmospheric Gases Experiment (AGAGE), Japan Meteorological Agency (JMA), etc., were obtained from the World Data Centre for Greenhouse Gases (<https://gaw.kishou.go.jp>) and the Global Environmental Database (<https://db.cger.nies.go.jp>). All observations are reported on or linked to the WMOX2004 calibration scale.

For satellite CH<sub>4</sub> observations, we used two retrievals of GOSAT XCH<sub>4</sub> provided by National Institute for Environmental Studies in Japan and the University of Leicester in the UK (denoted as “GSNIES” and “GSUoL” respectively). Launched by the Japan Aerospace Exploration Agency (JAXA) in early 2009, GOSAT achieves a global coverage every 3 days with a swath of 750 km and a ground pixel with a diameter of approximately 10.5 km at nadir. The Thermal And Near-infrared Sensor for Carbon Observation – Fourier Transform Spectrometer (TANSO-FTS) onboard enables the measurements of column-averaged dry-air CO<sub>2</sub> and CH<sub>4</sub> mole fractions by solar backscatter in the shortwave infrared (SWIR) with near-unit sensitivity across the air column down to the surface<sup>63,64</sup>. The two GOSAT XCH<sub>4</sub> products used here differ in their algorithms to treat the scattering-induced issues in the retrieval of total column concentrations from spectral data. The GSNIES XCH<sub>4</sub> retrieval was produced using a full-physics algorithm to infer CH<sub>4</sub> column together with physical scattering properties of the atmosphere<sup>65,66</sup>. Alternatively, the GSUoL XCH<sub>4</sub> retrieval employed a proxy algorithm that simultaneously retrieves CH<sub>4</sub> and CO<sub>2</sub> columns using the absorption features around the wavelength of 1.6 μm to minimize the scattering effect on the retrieval<sup>67,68</sup>. While the two conceptually different approaches have their own advantages and disadvantages<sup>69</sup>, the proxy retrieval is less sensitive to aerosol distribution and instrumental issues than the full-physics retrieval, therefore has much higher data density over geographic regions with substantial aerosol loading, such as in the tropics (Fig. S3). In this study, we used the GSNIES XCH<sub>4</sub> retrieval version 2.95/2.96<sup>12</sup> and the GSUoL XCH<sub>4</sub> retrieval version 9.0<sup>13</sup>, which are bias-corrected and in good agreement with ground-based XCH<sub>4</sub> measurements from the Total Column Carbon Observing Network (TCCON) and aircraft-based CH<sub>4</sub> profile measurements. These two retrievals have been widely used in global or regional methane inverse modeling to study recent trends and interannual variabilities<sup>7,9,54,55,70</sup>. Note that only retrievals over land (except those over Greenland; Fig. S3) were assimilated in our inversions in order to avoid potential retrieval biases between nadir and glint viewing modes.

To calculate atmospheric CH<sub>4</sub> growth rates in Figs. 1 and S1, for surface observations, we used zonally-averaged marine boundary layer (MBL) references for CH<sub>4</sub> constructed by NOAA’s Global Monitoring Laboratory (NOAA/GML) using measurements of weekly air samples from a subset of sites in the NOAA Cooperative Global Air Sampling Network<sup>11</sup>. Only sites that measure background atmospheric compositions are considered, typically at remote marine sea level locations with prevailing onshore winds (see the site map at <https://gml.noaa.gov/ccgg/mb1/map.php?param=CH4>). For GOSAT XCH<sub>4</sub> observations, we used daily means of all valid land retrievals per 10° latitude band between 50°N and 50°S for subsequent growth rate calculation. Note that GOSAT XCH<sub>4</sub> retrievals north of 50°N or south of 50°S were discarded for the calculation of growth rates due to data gaps over these regions during winter, but these data were included in atmospheric inversions (Fig. S3). The smoothed CH<sub>4</sub> growth rates for each latitude band shown in Fig. 1 and S1 were extracted from time series of the zonally-averaged MBL CH<sub>4</sub> references or GOSAT XCH<sub>4</sub> observations over the period 2010–2021 following the curve fitting procedures of ref. 71.

### Atmospheric 3D inversions

We used a variational Bayesian inversion system PYVAR-LMDZ-SACS (PYthon VARiational–Laboratoire de Météorologie Dynamique model with Zooming capability–Simplified Atmospheric Chemistry

System)<sup>14,15</sup> to optimize weekly CH<sub>4</sub> surface fluxes at a spatial resolution of 1.9° in latitude by 3.75° in longitude over the period 2019–2021. An ensemble of six inversions was performed (Table S1), using three different observation datasets described above as constraints, combined with two physical parameterizations for the transport model Laboratoire de Météorologie Dynamique with zooming capability (LMDZ), the atmospheric component of the coupled IPSL climate model participating in IPCC Assessment Reports (AR). These setups allowed us to explore consistency of the emission change patterns informed by different observation datasets while accounting for some of the uncertainties in atmospheric transport. The two physical parameterizations, denoted here as the “classic” and “advanced” versions, represent two development stages of LMDZ for IPCC AR3 and AR6<sup>72–74</sup>. The “classic” AR3 version<sup>72</sup> uses the vertical diffusion scheme of ref. 75 to represent the turbulent transport in the boundary layer and the scheme of ref. 76 to parameterize deep convection. The “advanced” AR6 version<sup>74</sup> combines the vertical diffusion scheme of ref. 77 and the thermal plume model by ref. 78 to simulate the atmospheric mixing in the boundary layer, and the deep convection is represented using the scheme of ref. 79 coupled with the parameterization of cold pools developed in ref. 80. While the “advanced” version showed overall improved representation of boundary layer mixing and large-scale atmospheric transport<sup>81–83</sup>, which would benefit trace gas transport simulations and inversions despite its comparatively larger computational costs, the “classic” version or its physical parameterization schemes are still widely used in the scientific community for methane studies (see Table S8 and S10 in ref. 84). A previous study<sup>85</sup> showed that changing physical parameterizations would have small impact on the inverted methane emissions at the global scale (around 1%), but could lead to significant differences in the north–south gradient of emissions and the emission partitioning between regions (also see Table S6).

Depending on the observations assimilated and the physical parameterizations used in the inversion system, discrepancies in the derived emission changes do exist among inversions at global or regional scales. The emission growth inferred from surface observations was much lower than those from GOSAT-based inversions for 2020 (Fig. S5a), possibly because surface networks have limited spatial coverage over certain key source regions (e.g., the tropics), thus being blind to the methane growth there (Fig. S2). Among the four GOSAT-based inversions, the ones constrained by GSUoL retrievals always gave 15–30% higher global net emission increases than those constrained by GSNIES retrievals (Fig. S5a, b), consistent with the steeper rise of the methane growth rate seen from GSUoL (Figs. 1 and S1). For several important emitting regions such as eastern China, northern India and southern Africa, the directions of emission changes disagreed among inversions assimilating different observations (Figs. S6 and S7), reflecting uncertainties in flux solution related to sparse data density or GOSAT XCH<sub>4</sub> retrieval algorithms. Note that we did not adjust GOSAT XCH<sub>4</sub> retrievals in our inversions. We acknowledge the inconsistency between surface-based and GOSAT-based inversions regarding the inferred global total emissions and their latitudinal gradients (Table S6; also see refs. 55,85–87), likely due to systematic biases in GOSAT retrievals and/or model representation of the stratospheric methane. Several previous studies applied an empirical bias correction on GOSAT retrievals, making the optimized atmospheric CH<sub>4</sub> more consistent with surface observations<sup>85,87–89</sup>. As our study focuses on the year-to-year changes of the optimized methane fluxes, which would be less sensitive to aforementioned systematic biases, we did not apply such an adjustment to GOSAT retrievals in our inversions (also see ref. 55).

Other configurations of the inversions followed the descriptions in ref. 8. The prior CH<sub>4</sub> fluxes were built on bottom-up inventories or process-based land surface models for different categories (Table S7), consistent with the priors used for top-down inversions contributing

to the new global methane budget (GMB) assessment<sup>84</sup>, which allows for comparisons with earlier studies and other modeling work within the GMB framework. The OH and O(<sup>1</sup>D) fields were prescribed from the simulation of a chemistry-climate model LMDZ-INCA (Laboratoire de Météorologie Dynamique model with Zooming capability – Interaction with Chemistry and Aerosols) with a full tropospheric photochemistry scheme<sup>16,17</sup>. The model was run at the resolution of 1.27° in latitude by 2.5° in longitude, driven by interannually varying horizontal winds from ECMWF ERA5 reanalysis<sup>18</sup> and with natural and anthropogenic emissions of NO<sub>x</sub>, CO and hydrocarbons updated to 2021 (refs. 19–21). As countries relaxed and lifted COVID-19 restrictions, global NO<sub>x</sub> emissions started to rebound in spring 2021, but annual emissions were still lower by 3–4% compared to 2019 (Fig. S4a–c; Table S2). Variations in CO emissions are dominated by biomass burning. While global CO emissions declined by about 12% in 2020 compared to 2019 because of less fire emissions in the Southern Hemisphere, emissions in 2021 were quite similar to the 2019 level. The reduced CO emissions in the Southern Hemisphere were sustained in 2021 but offset by abnormally high boreal fire emissions during summertime (Fig. S4d–f; Table S2)<sup>38</sup>. Our chemistry transport model LMDZ-INCA simulated a reduction of global tropospheric OH by 3% in 2021 relative to 2019, more than the 1.6–1.8% decrease in 2020 reported by ref. 8. Note that the resulting oxidant fields were not adjusted in the inversions in order to keep the simulated OH changes from LMDZ-INCA. We acknowledge that the reduced atmospheric sink could play an important role in the record high CH<sub>4</sub> growth rates during 2020–2021, although the attribution between changes in sources and sinks is still under debate<sup>4,7–9,90</sup>. While the changes in global tropospheric OH were broadly consistent with independent estimates and other studies for 2020<sup>7–9,91</sup>, the simulated OH change for 2021 could be more uncertain due to e.g. inaccurate emission forcings<sup>92</sup>, thereby complicating attribution of the anomalous CH<sub>4</sub> growth rates between sources and sinks. However, the dominant contribution from tropical regions to recent CH<sub>4</sub> emission surges was confirmed by other top-down studies using different inversion systems and OH configurations<sup>7,9</sup>.

The preprocessing of surface CH<sub>4</sub> observations and the assignment of observation errors were based on the protocol described in ref. 8. For continuous CH<sub>4</sub> measurements in particular, we calculated daily afternoon averages (12:00–16:00 local sidereal time, LST) for stations situated below 1000 meters above sea level (a.s.l.) and morning averages (0:00–4:00 LST) for stations located above 1000 meters a.s.l., which were used in subsequent inversion analyses. The observation errors are comprised of measurement errors, representation errors, and model errors. The latter two were approximated using the synoptic variability of CH<sub>4</sub> observations at each station, calculated as the residual standard deviation (RSD) of the de-trended and de-seasonalized observations<sup>85,93</sup>. For GOSAT XCH<sub>4</sub> observations, the valid data were averaged into model grids for each time step (30 mins) to create “super-observations”, with the observation errors defined as the retrieval errors reported by the data product plus model errors whose standard deviations were empirically set as 1% (refs. 55,93).

### Bottom-up estimates of methane emissions

Anthropogenic methane emissions were compiled from a combination of existing inventories. For the 42 Annex-I countries that report their national greenhouse gas inventories (NGHGs) to UNFCCC each year, we used the reported anthropogenic methane emissions updated to 2021 from coal mining, oil and gas production, agriculture and waste sectors, respectively (<https://unfccc.int/ghg-inventories-annex-i-parties/2023#fn2>). For China, anthropogenic methane emissions were computed and updated to 2021 based on the activity data collected from national statistic books<sup>94</sup> and specific emission factors at provincial levels<sup>95,96</sup>. For other countries, emissions from coal mining, oil and gas production, agriculture and waste were obtained from the

Emissions Database for Global Atmospheric Research version 7.0 (EDGAR v7.0)<sup>97,98</sup>, with coal production and livestock data corrected by the activity data from International Energy Agency (IEA)<sup>99</sup> and Food and Agriculture Organization of the United Nations (FAO)<sup>100</sup>. The national total emissions from the 42 Annex-I countries, China and other countries were distributed on 0.1° × 0.1° grid cells based on the spatial patterns of EDGAR v7.0. Note that the change in global anthropogenic methane emissions between 2020 and 2019 slightly differs from that reported by ref. 8, as different versions of EDGAR and IEA data were used in this study to estimate emissions.

The global fire methane emissions were obtained from the Global Fire Emissions Database version 4.1 including small fire burned area<sup>21,101</sup>. The data set produces monthly gridded burned area and fire emissions at a spatial resolution of 0.25° × 0.25°, based on satellite information on fire activity and vegetation productivity<sup>21</sup>.

For wetland emissions, we used two process-based wetland emission models (WEMs), ORCHIDEE-MICT<sup>102</sup> and LPJ-wsl<sup>103</sup>, to simulate the global wetland CH<sub>4</sub> emissions. Both ORCHIDEE-MICT and LPJ-wsl participated in the Wetland and Wetland CH<sub>4</sub> Inter-comparison of Models Project<sup>104,105</sup>, and have contributed to wetland biogeochemical model simulations of the Global Methane Budget<sup>84,106,107</sup>. These two models differ in model structures and parameterizations, and represent part of the wide uncertainty range in characterizing CH<sub>4</sub> emission processes<sup>104,105</sup>. An inter-comparison among GMB wetland model ensemble shows that ORCHIDEE-MICT and LPJ-wsl cover a considerable uncertainty range across the GMB wetland model ensemble in simulating global annual wetland CH<sub>4</sub> emissions and emission changes from 2019 to 2020, and broadly agree with the interannual variability of model ensemble means (Fig. S15). Based on the simulation protocol in ref. 8, wetland methane emissions were updated to 2021 using these two WEMs with four climate datasets (i.e., CRU TSv4.06<sup>108</sup>, ERA5<sup>18</sup>, MERRA2<sup>109</sup>, and MSWEPv2.8<sup>110,111</sup>) to account for uncertainties in simulating wetland CH<sub>4</sub> emissions due to meteorological forcings<sup>34</sup>. The spatiotemporal dynamics of wetland areas were simulated by a TOPMODEL-based diagnostic model and applied to ORCHIDEE-MICT<sup>112,113</sup> and LPJ-wsl<sup>114</sup>, respectively. For ORCHIDEE-MICT in particular, we utilized two wetland maps to calibrate the parameters in simulating the wetland area dynamics<sup>113</sup>. The static map of Regularly Flooded Wetlands (RFW)<sup>23</sup> was applied for the grid-based calibration of the long-term maximum wetland extent, whereas the Global Inundation Estimate from Multiple Satellites version 2 (GIEMS-2)<sup>115</sup> was applied to calibrate the yearly maximum wetland extent for each grid. Combining two wetland maps for ORCHIDEE-MICT and one for LPJ-wsl with four climate datasets, we included a total of twelve simulations of wetland CH<sub>4</sub> in our analyses (Fig. S11).

### Data availability

The datasets that support the findings of this study are publicly available as follows. The global atmospheric methane growth rates and marine boundary layer references are obtained from [https://gml.noaa.gov/ccgg/trends\\_ch4](https://gml.noaa.gov/ccgg/trends_ch4) and <https://gml.noaa.gov/ccgg/mbl/> respectively. The assimilated surface CH<sub>4</sub> observations from NOAA and ICOS networks are available at <https://doi.org/10.15138/VNCZ-M766> and <https://doi.org/10.18160/KCYX-HA35>; surface observations from other networks are available from World Data Centre for Greenhouse Gases (<https://gaw.kishou.go.jp/>) and Global Environmental Database (<https://db.cger.nies.go.jp/>). The GOSAT NIES full physics XCH<sub>4</sub> retrievals are available at <https://data2.gosat.nies.go.jp/> through registration; the GOSAT University of Leicester proxy XCH<sub>4</sub> retrievals are available at <https://catalogue.ceda.ac.uk/uuid/18ef8247f52a4cb6a14013f8235cc1eb>. The EDGAR v7.0 time series of country-level emissions and sector-specific gridmaps are downloaded from [https://edgar.jrc.ec.europa.eu/dataset\\_ghg70](https://edgar.jrc.ec.europa.eu/dataset_ghg70). The hourly ERA5 reanalysis data are obtained from <https://www.ecmwf.int/en/forecasts/dataset/ecmwf-reanalysis-v5>. The monthly datasets of temperature and



precipitation from CRU TS v4.06 are obtained from [https://crudata.uea.ac.uk/cru/data/hrg/cru\\_ts\\_4.06/](https://crudata.uea.ac.uk/cru/data/hrg/cru_ts_4.06/). The monthly precipitation data from MERRA2 are obtained from <https://gmao.gsfc.nasa.gov/reanalysis/MERRA-2/>. The monthly precipitation data from MSWEP v2.8 are obtained from <http://www.gloh2o.org/mswep/>. The dataset of monthly global water storage/height anomalies from GRACE-FO is available at <https://doi.org/10.5067/TEMSC-3JC63>. The Regular Flooded Wetlands maps are available at <https://doi.pangaea.de/10.1594/PANGAEA.892657>. The monthly wetland extents based on CYGNSS observations are obtained from the Berkeley-RWAWC product available at [https://podaac.jpl.nasa.gov/dataset/CYGNSS\\_L3\\_UC\\_BERKELEY\\_WATERMASK\\_V3.1](https://podaac.jpl.nasa.gov/dataset/CYGNSS_L3_UC_BERKELEY_WATERMASK_V3.1). The monthly fire emissions from Global Fire Emissions Database version 4.1, which includes small fire burned area, are obtained from <https://www.geo.vu.nl/~gwerf/GFED/GFED4/>. The anthropogenic emissions from the CEDS emission inventory up to 2019 are available at <https://data.pnnl.gov/dataset/CEDS-4-21-21>. The gridded near-real time fossil fuel combustion data that include confinement-induced reductions in 2020 and rebound in 2021 are obtained from <https://carbonmonitor.org/>. The global gridded anthropogenic CH<sub>4</sub> emissions and the outputs of WEMs, LMDZ-INCA and atmospheric inversions are publicly available at Figshare (<https://doi.org/10.6084/m9.figshare.27207999.v1>). Source data are provided with this paper.

### Code availability

The codes and documentation for the process-based wetland model ORCHIDEE-MICT (v8.4.4) are publicly available at <http://forge.ipsl.fr/orchidee/>; the LPJ-wsl model code is freely available at [https://github.com/benpoulter/LPJ-wsl\\_v2.0.git](https://github.com/benpoulter/LPJ-wsl_v2.0.git), and a permanent version of the model code is deposited at Zenodo (<https://doi.org/10.5281/zenodo.4409331>). The global chemistry transport model LMDZ-INCA is part of the coupled IPSL climate model, with its codes and documentation available at <https://cmc.ipsl.fr/ipsl-climate-models/ipsl-cm6/>. The codes for the atmospheric inversion system are publicly available at <http://community-inversion.eu/installation.html#getting-the-code>.

### References

- Lan, X., Thoning, K. W. & Dlugokencky, E. J. *Trends in globally-averaged CH<sub>4</sub>, N<sub>2</sub>O, and SF<sub>6</sub> determined from NOAA Global Monitoring Laboratory measurements* (version 2023-03, accessed 1 May 2023); [https://gml.noaa.gov/ccgg/trends\\_ch4](https://gml.noaa.gov/ccgg/trends_ch4).
- Davis, S. J. et al. Emissions rebound from the COVID-19 pandemic. *Nat. Clim. Chang.* **12**, 412–414 (2022).
- Jackson, R. B. et al. Global fossil carbon emissions rebound near pre-COVID-19 levels. *Environ. Res. Lett.* **17**, 031001 (2022).
- Laughner, J. L. et al. Societal shifts due to COVID-19 reveal large-scale complexities and feedbacks between atmospheric chemistry and climate change. *Proc. Natl Acad. Sci. USA* **118**, e2109481118 (2021).
- Miyazaki, K. et al. Global tropospheric ozone responses to reduced NO<sub>x</sub> emissions linked to the COVID-19 worldwide lockdowns. *Sci. Adv.* **7**, eabf7460 (2021).
- Li, X., Hu, Z.-Z., Tseng, Y., Liu, Y. & Liang, P. A historical perspective of the La Niña event in 2020/2021. *J. Geophys. Res. Atmos.* **127**, e2021JD035546 (2022).
- Feng, L., Palmer, P. I., Parker, R. J., Lunt, M. F. & Bösch, H. Methane emissions are predominantly responsible for record-breaking atmospheric methane growth rates in 2020 and 2021. *Atmos. Chem. Phys.* **23**, 4863–4880 (2023).
- Peng, S. et al. Wetland emission and atmospheric sink changes explain methane growth in 2020. *Nature* **612**, 477–482 (2022).
- Qu, Z. et al. Attribution of the 2020 surge in atmospheric methane by inverse analysis of GOSAT observations. *Environ. Res. Lett.* **17**, 094003 (2022).
- Zhang, Z. et al. Recent intensification of wetland methane feedback. *Nat. Clim. Chang.* **13**, 430–433 (2023).
- Lan, X., Tans, P. P., Thoning, K. W. & NOAA Global Monitoring Laboratory. *NOAA Greenhouse Gas Marine Boundary Layer Reference – CH<sub>4</sub>* (accessed 1 July 2023); <https://doi.org/10.15138/TJQP-OD69>.
- Inoue, M. et al. Bias corrections of GOSAT SWIR XCO<sub>2</sub> and XCH<sub>4</sub> with TCCON data and their evaluation using aircraft measurement data. *Atmos. Meas. Tech.* **9**, 3491–3512 (2016).
- Parker, R. J. et al. A decade of GOSAT Proxy satellite CH<sub>4</sub> observations. *Earth Syst. Sci. Data* **12**, 3383–3412 (2020).
- Chevallier, F. et al. Inferring CO<sub>2</sub> sources and sinks from satellite observations: Method and application to TOVS data. *J. Geophys. Res. Atmos.* **110**, D24309 (2005).
- Pison, I., Bousquet, P., Chevallier, F., Szopa, S. & Hauglustaine, D. Multi-species inversion of CH<sub>4</sub>, CO and H<sub>2</sub> emissions from surface measurements. *Atmos. Chem. Phys.* **9**, 5281–5297 (2009).
- Hauglustaine, D. A. et al. Interactive chemistry in the Laboratoire de Météorologie Dynamique general circulation model: Description and background tropospheric chemistry evaluation. *J. Geophys. Res. Atmos.* **109**, D04314 (2004).
- Hauglustaine, D. A., Balkanski, Y. & Schulz, M. A global model simulation of present and future nitrate aerosols and their direct radiative forcing of climate. *Atmos. Chem. Phys.* **14**, 11031–11063 (2014).
- Hersbach, H. et al. ERA5 Hourly Data on Single Levels from 1940 to Present (Copernicus Climate Change Service, Climate Data Store, accessed 1 March 2022); <https://doi.org/10.24381/cds.adbb2d47>.
- Carbon Monitor (accessed 1 Oct 2022); <https://carbonmonitor.org>.
- Community Emissions Data System (CEDS). *CEDS v\_2021\_04\_21 Gridded Emissions Data (PNNL)*, accessed <https://data.pnnl.gov/dataset/CEDS-4-21-21> (1 Oct 2022).
- van der Werf, G. R. et al. Global fire emissions estimates during 1997–2016. *Earth Syst. Sci. Data* **9**, 697–720 (2017).
- Bloom, A. A., Palmer, P. I., Fraser, A., Reay, D. S. & Frankenberg, C. Large-scale controls of methanogenesis inferred from methane and gravity spaceborne data. *Science* **327**, 322–325 (2010).
- Tootchi, A., Jost, A. & Ducharme, A. Multi-source global wetland maps combining surface water imagery and groundwater constraints. *Earth Syst. Sci. Data* **11**, 189–220 (2019).
- Zheng, B. et al. Global atmospheric carbon monoxide budget 2000–2017 inferred from multi-species atmospheric inversions. *Earth Syst. Sci. Data* **11**, 1411–1436 (2019).
- Fleischmann, A. S. et al. Increased floodplain inundation in the Amazon since 1980. *Environ. Res. Lett.* **18**, 034024 (2023).
- Barichivich, J. et al. Recent intensification of Amazon flooding extremes driven by strengthened Walker circulation. *Sci. Adv.* **4**, eaat8785 (2018).
- Espinoza, J.-C., Marengo, J. A., Schongart, J. & Jimenez, J. C. The new historical flood of 2021 in the Amazon River compared to major floods of the 21st century: Atmospheric features in the context of the intensification of floods. *Weather Clim. Extrem.* **35**, 100406 (2022).
- Calim Costa, M., Marengo, J. A., Alves, L. M. & Cunha, A. P. Multiscale analysis of drought, heatwaves, and compound events in the Brazilian Pantanal in 2019–2021. *Theor. Appl. Climatol.* **155**, 661–677 (2024).
- Espínola, L. A. et al. Application of ecohydrological criteria for the management of fisheries in the middle Paraná River (Argentina) during extreme low water levels. *Ecohydrology* **17**, e2600 (2024).
- Marengo, J. A. et al. Extreme drought in the Brazilian Pantanal in 2019–2020: Characterization, causes, and impacts. *Front. Water* **3**, 639204 (2021).

31. Lyon, B. & Barnston, A. G. ENSO and the spatial extent of inter-annual precipitation extremes in tropical land areas. *J. Clim.* **18**, 5095–5109 (2005).
32. Hodson, E. L., Poulter, B., Zimmermann, N. E., Prigent, C. & Kaplan, J. O. The El Niño–Southern Oscillation and wetland methane interannual variability. *Geophys. Res. Lett.* **38**, L08810 (2011).
33. Pandey, S. et al. Enhanced methane emissions from tropical wetlands during the 2011 La Niña. *Sci. Rep.* **7**, 45759 (2017).
34. Zhang, Z. et al. Enhanced response of global wetland methane emissions to the 2015–2016 El Niño–Southern Oscillation event. *Environ. Res. Lett.* **13**, 074009 (2018).
35. Zhu, Q. et al. Interannual variation in methane emissions from tropical wetlands triggered by repeated El Niño Southern Oscillation. *Glob. Change Biol.* **23**, 4706–4716 (2017).
36. Mason, S. J. & Goddard, L. Probabilistic precipitation anomalies associated with ENSO. *Bull. Am. Meteorol. Soc.* **82**, 619–638 (2001).
37. Schaefer, H. et al. Limited impact of El Niño–Southern Oscillation on variability and growth rate of atmospheric methane. *Biogeosciences* **15**, 6371–6386 (2018).
38. Zheng, B. et al. Record-high CO<sub>2</sub> emissions from boreal fires in 2021. *Science* **379**, 912–917 (2023).
39. Lunt, M. F. et al. An increase in methane emissions from tropical Africa between 2010 and 2016 inferred from satellite data. *Atmos. Chem. Phys.* **19**, 14721–14740 (2019).
40. Lunt, M. F. et al. Rain-fed pulses of methane from East Africa during 2018–2019 contributed to atmospheric growth rate. *Environ. Res. Lett.* **16**, 024021 (2021).
41. Pandey, S. et al. Using satellite data to identify the methane emission controls of South Sudan’s wetlands. *Biogeosciences* **18**, 557–572 (2021).
42. Bloom, A. A., Palmer, P. I., Fraser, A. & Reay, D. S. Seasonal variability of tropical wetland CH<sub>4</sub> emissions: the role of the methanogen-available carbon pool. *Biogeosciences* **9**, 2821–2830 (2012).
43. Gerlein-Safdi, C., Bloom, A. A., Plant, G., Kort, E. A. & Ruf, C. S. Improving representation of tropical wetland methane emissions with CYGNSS inundation maps. *Glob. Biogeochem. Cycles* **35**, e2020GB006890 (2021).
44. Pu, T. et al. Berkeley-RWAWC: A new CYGNSS-based watermask unveils unique observations of seasonal dynamics in the Tropics. *Water Resour. Res.* **60**, e2024WR037060 (2024).
45. Parker, R. J. et al. Evaluating year-to-year anomalies in tropical wetland methane emissions using satellite CH<sub>4</sub> observations. *Remote Sens. Environ.* **211**, 261–275 (2018).
46. Parker, R. J. et al. Evaluation of wetland CH<sub>4</sub> in the Joint UK Land Environment Simulator (JULES) land surface model using satellite observations. *Biogeosciences* **19**, 5779–5805 (2022).
47. Pangala, S. R. et al. Large emissions from floodplain trees close the Amazon methane budget. *Nature* **552**, 230–234 (2017).
48. Shaw, J. T. et al. Large methane emission fluxes observed from tropical wetlands in Zambia. *Glob. Biogeochem. Cycles* **36**, e2021GB007261 (2022).
49. Delwiche, K. B. et al. FLUXNET-CH<sub>4</sub>: a global, multi-ecosystem dataset and analysis of methane seasonality from freshwater wetlands. *Earth Syst. Sci. Data* **13**, 3607–3689 (2021).
50. Knox, S. H. et al. FLUXNET-CH<sub>4</sub> synthesis activity: Objectives, observations, and future directions. *Bull. Am. Meteorol. Soc.* **100**, 2607–2632 (2019).
51. Gauci, V. et al. Non-flooded riparian Amazon trees are a regionally significant methane source. *Philos. Trans. R. Soc. Math. Phys. Eng. Sci.* **380**, 20200446 (2021).
52. Gedney, N., Huntingford, C., Comyn-Platt, E. & Wiltshire, A. Significant feedbacks of wetland methane release on climate change and the causes of their uncertainty. *Environ. Res. Lett.* **14**, 084027 (2019).
53. Feng, L., Palmer, P. I., Zhu, S., Parker, R. J. & Liu, Y. Tropical methane emissions explain large fraction of recent changes in global atmospheric methane growth rate. *Nat. Commun.* **13**, 1378 (2022).
54. Wilson, C. et al. Large and increasing methane emissions from eastern Amazonia derived from satellite data, 2010–2018. *Atmos. Chem. Phys.* **21**, 10643–10669 (2021).
55. Yin, Y. et al. Accelerating methane growth rate from 2010 to 2017: leading contributions from the tropics and East Asia. *Atmos. Chem. Phys.* **21**, 12631–12647 (2021).
56. Yuan, K. et al. Boreal–Arctic wetland methane emissions modulated by warming and vegetation activity. *Nat. Clim. Chang.* **14**, 282–288 (2024).
57. Nisbet, E. G. Climate feedback on methane from wetlands. *Nat. Clim. Chang.* **13**, 421–422 (2023).
58. Cai, W. et al. Increased frequency of extreme La Niña events under greenhouse warming. *Nat. Clim. Chang.* **5**, 132–137 (2015).
59. Geng, T. et al. Increased occurrences of consecutive La Niña events under global warming. *Nature* **619**, 774–781 (2023).
60. Thompson, R. L. Climate feedback from wetland emissions of methane may necessitate greater anthropogenic reductions. *AGU Adv.* **2**, e2021AV000533 (2021).
61. Lan, X. et al. Atmospheric Methane Dry Air Mole Fractions from the NOAA GML Carbon Cycle Cooperative Global Air Sampling Network, 1983–2021 (accessed 1 Oct 2022); <https://doi.org/10.15138/VNCZ-M766>.
62. ICOS RI et al. ICOS Atmosphere Release 2022–1 of Level 2 Greenhouse Gas Mole Fractions of CO<sub>2</sub>, CH<sub>4</sub>, N<sub>2</sub>O, CO, Meteorology and <sup>14</sup>CO<sub>2</sub>. <https://doi.org/10.18160/KCYX-HA35> (accessed 1 Oct 2022).
63. Butz, A. et al. Toward accurate CO<sub>2</sub> and CH<sub>4</sub> observations from GOSAT. *Geophys. Res. Lett.* **38**, L14812 (2011).
64. Kuze, A., Suto, H., Nakajima, M. & Hamazaki, T. Thermal and near infrared sensor for carbon observation Fourier-transform spectrometer on the Greenhouse Gases Observing Satellite for greenhouse gases monitoring. *Appl. Opt.* **48**, 6716–6733 (2009).
65. Yoshida, Y. et al. Retrieval algorithm for CO<sub>2</sub> and CH<sub>4</sub> column abundances from short-wavelength infrared spectral observations by the greenhouse gases observing satellite. *Atmos. Meas. Tech.* **4**, 717–734 (2011).
66. Yoshida, Y. et al. Improvement of the retrieval algorithm for GOSAT SWIR XCO<sub>2</sub> and XCH<sub>4</sub> and their validation using TCCON data. *Atmos. Meas. Tech.* **6**, 1533–1547 (2013).
67. Parker, R. et al. Methane observations from the Greenhouse Gases Observing Satellite: Comparison to ground-based TCCON data and model calculations. *Geophys. Res. Lett.* **38**, L15807 (2011).
68. Parker, R. J. et al. Assessing 5 years of GOSAT Proxy XCH<sub>4</sub> data and associated uncertainties. *Atmos. Meas. Tech.* **8**, 4785–4801 (2015).
69. Schepers, D. et al. Methane retrievals from Greenhouse Gases Observing Satellite (GOSAT) shortwave infrared measurements: Performance comparison of proxy and physics retrieval algorithms. *J. Geophys. Res. Atmos.* **117**, D10307 (2012).
70. Wang, F. et al. Interannual variability on methane emissions in monsoon Asia derived from GOSAT and surface observations. *Environ. Res. Lett.* **16**, 024040 (2021).
71. Thoning, K. W., Tans, P. P. & Komhyr, W. D. Atmospheric carbon dioxide at Mauna Loa Observatory: 2. Analysis of the NOAA GMCC data, 1974–1985. *J. Geophys. Res. Atmos.* **94**, 8549–8565 (1989).
72. Hourdin, F. et al. The LMDZ4 general circulation model: climate performance and sensitivity to parametrized physics with emphasis on tropical convection. *Clim. Dyn.* **27**, 787–813 (2006).
73. Hourdin, F. et al. LMDZ5B: the atmospheric component of the IPSL climate model with revisited parameterizations for clouds and convection. *Clim. Dyn.* **40**, 2193–2222 (2013).

74. Hourdin, F. et al. LMDZ6A: The atmospheric component of the IPSL climate model with improved and better tuned physics. *J. Adv. Model. Earth Syst.* **12**, e2019MS001892 (2020).
75. Louis, J.-F. A parametric model of vertical eddy fluxes in the atmosphere. *Bound.-Layer. Meteorol.* **17**, 187–202 (1979).
76. Tiedtke, M. A comprehensive mass flux scheme for cumulus parameterization in large-scale models. *Mon. Weather Rev.* **117**, 1779–1800 (1989).
77. Mellor, G. L. & Yamada, T. A hierarchy of turbulence closure models for planetary boundary layers. *J. Atmos. Sci.* **31**, 1791–1806 (1974).
78. Rio, C. & Hourdin, F. A thermal plume model for the convective boundary layer: Representation of cumulus clouds. *J. Atmos. Sci.* **65**, 407–425 (2008).
79. Emanuel, K. A. A scheme for representing cumulus convection in large-scale models. *J. Atmos. Sci.* **48**, 2313–2329 (1991).
80. Grandpeix, J.-Y., Lafore, J.-P. & Cheruy, F. A density current parameterization coupled with Emanuel’s convection scheme. Part II: 1D simulations. *J. Atmos. Sci.* **67**, 898–922 (2010).
81. Locatelli, R. et al. Atmospheric transport and chemistry of trace gases in LMDz5B: evaluation and implications for inverse modeling. *Geosci. Model Dev.* **8**, 129–150 (2015).
82. Remaud, M., Chevallier, F., Cozic, A., Lin, X. & Bousquet, P. On the impact of recent developments of the LMDz atmospheric general circulation model on the simulation of CO<sub>2</sub> transport. *Geosci. Model Dev.* **11**, 4489–4513 (2018).
83. Remaud, M. et al. Intercomparison of atmospheric carbonyl sulfide (TransCom-COS; Part One): Evaluating the impact of transport and emissions on tropospheric variability using ground-based and aircraft data. *J. Geophys. Res. Atmos.* **128**, e2022JD037817 (2023).
84. Saunois, M. et al. Global Methane Budget 2000–2020. *Earth Syst. Sci. Data Discuss.* 1–147 <https://doi.org/10.5194/essd-2024-115> (2024).
85. Locatelli, R., Bousquet, P., Saunois, M., Chevallier, F. & Cressot, C. Sensitivity of the recent methane budget to LMDz sub-grid-scale physical parameterizations. *Atmos. Chem. Phys.* **15**, 9765–9780 (2015).
86. Bergamaschi, P. et al. Inverse modeling of global and regional CH<sub>4</sub> emissions using SCIAMACHY satellite retrievals. *J. Geophys. Res. Atmos.* **114**, (2009).
87. Turner, A. J. et al. Estimating global and North American methane emissions with high spatial resolution using GOSAT satellite data. *Atmos. Chem. Phys.* **15**, 7049–7069 (2015).
88. Fraser, A. et al. Estimating regional methane surface fluxes: the relative importance of surface and GOSAT mole fraction measurements. *Atmos. Chem. Phys.* **13**, 5697–5713 (2013).
89. Alexe, M. et al. Inverse modelling of CH<sub>4</sub> emissions for 2010–2011 using different satellite retrieval products from GOSAT and SCIAMACHY. *Atmos. Chem. Phys.* **15**, 113–133 (2015).
90. Stevenson, D. S., Derwent, R. G., Wild, O. & Collins, W. J. COVID-19 lockdown emission reductions have the potential to explain over half of the coincident increase in global atmospheric methane. *Atmos. Chem. Phys.* **22**, 14243–14252 (2022).
91. Thompson, R. L. et al. Estimation of the atmospheric hydroxyl radical oxidative capacity using multiple hydrofluorocarbons (HFCs). *Atmos. Chem. Phys.* **24**, 1415–1427 (2024).
92. Li, H. et al. Trends and drivers of anthropogenic NO<sub>x</sub> emissions in China since 2020. *Environ. Sci. Ecotechnol.* **21**, 100425 (2024).
93. Cressot, C. et al. On the consistency between global and regional methane emissions inferred from SCIAMACHY, TANSO-FTS, IASI and surface measurements. *Atmos. Chem. Phys.* **14**, 577–592 (2014).
94. National Bureau of Statistics of China. *China Statistical Yearbook* (accessed 1 Oct 2022); <https://www.stats.gov.cn/english/Statisticaldata/yearbook>.
95. Liu, G. et al. Recent slowdown of anthropogenic methane emissions in China driven by stabilized coal production. *Environ. Sci. Technol. Lett.* **8**, 739–746 (2021).
96. Peng, S. et al. Inventory of anthropogenic methane emissions in mainland China from 1980 to 2010. *Atmos. Chem. Phys.* **16**, 14545–14562 (2016).
97. Crippa, M. et al. *GHG Emissions of All World Countries: 2021 Report* (Publications Office of the European Union, 2021); <https://doi.org/10.2760/173513>.
98. Crippa, M. et al. *CO<sub>2</sub> Emissions of All World Countries – JRC/IEA/PBL 2022 Report* (Publications Office of the European Union, 2022); <https://doi.org/10.2760/730164>.
99. International Energy Agency. *World Energy Balances Highlights* (IEA, accessed 1 May 2023); <https://www.iea.org/data-and-statistics/data-product/world-energy-balances-highlights>.
100. Food and Agriculture Organization of the United Nations (FAO). *FAOSTAT Emissions Land Use Database* (accessed 1 May 2023); <https://www.fao.org/faostat/en/#data>.
101. Randerson, J. T., Chen, Y., van der Werf, G. R., Rogers, B. M. & Morton, D. C. Global burned area and biomass burning emissions from small fires. *J. Geophys. Res. Biogeosci.* **117**, (2012).
102. Guimberteau, M. et al. ORCHIDEE-MICT (v8.4.1), a land surface model for the high latitudes: model description and validation. *Geosci. Model Dev.* **11**, 121–163 (2018).
103. Zhang, Z. et al. Emerging role of wetland methane emissions in driving 21st century climate change. *Proc. Natl Acad. Sci. USA* **114**, 9647–9652 (2017).
104. Wania, R. et al. Present state of global wetland extent and wetland methane modelling: methodology of a model inter-comparison project (WETCHIMP). *Geosci. Model Dev.* **6**, 617–641 (2013).
105. Melton, J. R. et al. Present state of global wetland extent and wetland methane modelling: conclusions from a model inter-comparison project (WETCHIMP). *Biogeosciences* **10**, 753–788 (2013).
106. Saunois, M. et al. The Global Methane Budget 2000–2012. *Earth Syst. Sci. Data* **8**, 697–751 (2016).
107. Saunois, M. et al. The Global Methane Budget 2000–2017. *Earth Syst. Sci. Data* **12**, 1561–1623 (2020).
108. Harris, I., Osborn, T. J., Jones, P. & Lister, D. Version 4 of the CRU TS monthly high-resolution gridded multivariate climate dataset. *Sci. Data* **7**, 109 (2020).
109. Global Modeling and Assimilation Office (GMAO). *MERRA-2 tavg1\_2d\_flg\_Nx: 2d,1-Hourly, Time-Averaged, Single-Level, Assimilation, Surface Flux Diagnostics V5.12.4* (Goddard Space Flight Center Distributed Active Archive Center (GSFC DAAC), accessed 1 March 2022); <https://gmao.gsfc.nasa.gov/reanalysis/MERRA-2/>.
110. Beck, H. E. et al. MSWEP: 3-hourly 0.25° global gridded precipitation (1979–2015) by merging gauge, satellite, and reanalysis data. *Hydrol. Earth Syst. Sci.* **21**, 589–615 (2017).
111. Beck, H. E. et al. MSWEP V2 global 3-hourly 0.1° precipitation: methodology and quantitative assessment. *Bull. Am. Meteorol. Soc.* **100**, 473–500 (2019).
112. Xi, Y., Peng, S., Ciais, P. & Chen, Y. Future impacts of climate change on inland Ramsar wetlands. *Nat. Clim. Chang.* **11**, 45–51 (2021).
113. Xi, Y. et al. Gridded maps of wetlands dynamics over mid-low latitudes for 1980–2020 based on TOPMODEL. *Sci. Data* **9**, 347 (2022).
114. Zhang, Z., Zimmermann, N. E., Kaplan, J. O. & Poulter, B. Modeling spatiotemporal dynamics of global wetlands: comprehensive evaluation of a new sub-grid TOPMODEL parameterization and uncertainties. *Biogeosciences* **13**, 1387–1408 (2016).

115. Prigent, C., Jimenez, C. & Bousquet, P. Satellite-derived global surface water extent and dynamics over the last 25 years (GIEMS-2). *J. Geophys. Res. Atmos.* **125**, e2019JD030711 (2020).

## Acknowledgements

The study was funded by the ESA CCI RECCAP2 project (ESRIN/4000123002/18/I-NB). S.P. acknowledges the support from the National Natural Science Foundation of China (grant 42325102). P.C. acknowledges the support from the ANR CLAND convergence institute. R.J.P. and H.B. were funded via the UK National Centre for Earth Observation (grant nos. NE/R016518/1 and NE/N018079/1), as well as from the ESA GHG-CCI and Copernicus C3S projects (grant no. C3S2\_312a\_Lot2). R.J.P. is also funded via the UK National Centre for Earth Observation (Grant: NE/W004895/1) and UKRI Future Leaders Fellowship (Grant: MR/X033139/1). The GOSAT data generation was supported by the Natural Environment Research Council (NERC grant reference number: NE/X019071/1, “UK EO Climate Information Service”). We are very grateful to the scientists and technicians who are running surface networks of CH<sub>4</sub> observations and make these datasets available. We thank the Japanese Aerospace Exploration Agency, National Institute for Environmental Studies and the Ministry of Environment for the GOSAT data and their continuous support as part of the Joint Research Agreement. This research is supported through HPC resources of TGCC under the allocation A0110102201 made by GENCI for LMDZ-INCA simulations and computing mass fluxes, the Peking University supercomputing facility for ORCHIDEE-MICT simulations, and the ALICE high-performance computing facility at the University of Leicester for the GOSAT retrievals and analysis. We also acknowledge the technical support from the IT team of LSCE.

## Author contributions

X. Lin, S.P. and P.C. designed the study. X. Lin performed atmospheric 3D inversions, with precomputed mass fluxes prepared by M. Remaud, G.L. and S.P. built the bottom-up anthropogenic emissions inventory. S.P. and Y.X. performed ORCHIDEE simulations; Z.Z. and B.P. performed LPJ-wsl simulations. D.H. and B.Z. performed LMDZ-INCA simulations. M. Ramonet and X. Lan provided surface CH<sub>4</sub> observations; Y. Yoshida provided GOSAT NIES full physics XCH<sub>4</sub> retrievals; R.J.P. and H.B. provided GOSAT University of Leicester proxy XCH<sub>4</sub> retrievals. C.G.-S. and T.P. provided CYGNSS inundation maps. X. Lin coordinated the research and conducted the analyses; S.H. and B.D. help preprocess the data. X. Lin drafted the first manuscript; S.P., P.C., X. Lan, Y. Yin, Z.Z., H.B., P.B.,

F.C., C.G.-S., R.J.P, B.P., M. Remaud, A.R., M.S., R.L.T., Y. Yoshida and B.Z. contributed to writing and commenting on the draft manuscript.

## Competing interests

The authors declare no competing interests.

## Additional information

**Supplementary information** The online version contains supplementary material available at <https://doi.org/10.1038/s41467-024-55266-y>.

**Correspondence** and requests for materials should be addressed to Xin Lin.

**Peer review information** *Nature Communications* thanks Hinrich Schaefer, and the other, anonymous, reviewer(s) for their contribution to the peer review of this work. A peer review file is available.

**Reprints and permissions information** is available at <http://www.nature.com/reprints>

**Publisher's note** Springer Nature remains neutral with regard to jurisdictional claims in published maps and institutional affiliations.

**Open Access** This article is licensed under a Creative Commons Attribution-NonCommercial-NoDerivatives 4.0 International License, which permits any non-commercial use, sharing, distribution and reproduction in any medium or format, as long as you give appropriate credit to the original author(s) and the source, provide a link to the Creative Commons licence, and indicate if you modified the licensed material. You do not have permission under this licence to share adapted material derived from this article or parts of it. The images or other third party material in this article are included in the article's Creative Commons licence, unless indicated otherwise in a credit line to the material. If material is not included in the article's Creative Commons licence and your intended use is not permitted by statutory regulation or exceeds the permitted use, you will need to obtain permission directly from the copyright holder. To view a copy of this licence, visit <http://creativecommons.org/licenses/by-nc-nd/4.0/>.

© The Author(s) 2024